Boundary-Layer Meteorology (2005) 117: 275–300
DOI 10.1007/s10546-004-6005-0

OBSERVATIONS AND MODELLING OF COLD-AIR ADVECTION OVER ARCTIC SEA ICE

TIMO VIHMA[1,*], CHRISTOF LÜPKES[2], JÖRG HARTMANN[2] AND HANNU SAVIJÄRVI[3]

[1]*Finnish Institute of Marine Research, P.O. Box 33, FIN-00931 Helsinki, Finland;* [2]*Alfred Wegener Institute for Polar and Marine Research, Bremerhaven, Germany;* [3]*Division of Atmospheric Sciences, Department of Physical Sciences, University of Helsinki, Finland*

(Received in final form 24 May 2004)

Abstract. Aircraft observations of the atmospheric boundary layer (ABL) over Arctic sea ice were made during non-stationary conditions of cold-air advection with a cloud edge retreating through the study region. The sea-ice concentration, roughness, and ABL stratification varied in space. In the ABL heat budget, 80% of the Eulerian change in time was explained by cold-air advection and 20% by diabatic heating. With the cloud cover and inflow potential temperature profile prescribed as a function of time, the air temperature and near-surface fluxes of heat and momentum were well simulated by the applied two-dimensional mesoscale model. Model sensitivity tests demonstrated that several factors can be active in generating unstable stratification in the ABL over the Arctic sea ice in March. In this case, the upward sensible heat flux resulted from the combined effect of clouds, leads, and cold-air advection. These three factors interacted non-linearly with each other. From the point of view of ABL temperatures, the lead effect was far less important than the cloud effect, which influenced the temperature profiles via cloud-top radiative cooling and radiative heating of the snow surface. The steady-state simulations demonstrated that under overcast skies the evolution towards a deep, well-mixed ABL may take place through the merging of two mixed layers: one related to mostly shear-driven surface mixing and the other to buoyancy-driven top-down mixing due to cloud-top radiative cooling.

Keywords: Arctic, Cloud-top radiative cooling, Cold-air advection, Sea ice, Surface fluxes.

1. Introduction

The thermal stratification of the atmospheric boundary layer (ABL) over ice-covered Polar oceans varies in space and time. In winter, over sea ice, the radiation balance of the snow surface is usually negative and the ABL stratification is stable (Persson et al., 2002). The sensible heat flux is accordingly directed from air to snow, and its cooling effect on the ABL is, on the large scale, balanced by warm-air advection and subsidence (Overland and Turet, 1994). Several factors can, however, induce convection in the ABL. Large heat fluxes from leads and polynyas can result in localized convection (Schnell

* E-mail: vihma@fimr.fi

et al., 1989; Serrezze et al., 1992; Alam and Curry, 1997), as can also be the case over new, thin ice, which has a surface temperature between those of open leads and thick ice (Pinto et al., 2003). In winter, unstable stratification over a thick, compact (nearly 100% ice concentration) Arctic sea-ice cover is less common, but may occur in overcast conditions with enhanced downward longwave radiation from clouds (Intrieri et al., 2002). Furthermore, cloud-top radiative cooling may cause top-down mixing and generate a convective ABL even without any major surface heating (Pinto, 1998; Wang et al., 2001). Unstable stratification may also be generated due to cold-air advection over a warmer sea-ice surface (Vihma and Brümmer, 2002).

In summer, with a larger incoming solar radiation and a lower surface albedo, the ABL over sea ice can be slightly unstable even without the presence of the above-mentioned factors (although a cloud cover is usually present). In the project 'Surface Heat Budget of the Arctic Ocean' (SHEBA, Uttal et al., 2002), extensive boundary-layer measurements were made in 1997–1998 from a 20-m tower set on sea ice (Andreas et al., 1999). We made some simple calculations based on their sensible heat flux data at a height of 10 m: unstable stratification was most common in August (58% of the time) and least common in December and February (8%) (see also Figure 12 in Persson et al., 2002). In March–April 1998, around the period of this study, unstable stratification occurred for 31% of the time at the SHEBA observation site; the upward sensible heat flux was, however, never large: its maximum value was less than 20 W m^{-2}.

Most of our knowledge of turbulent fluxes and thermal stratification over sea ice is based on point measurements (e.g., Jordan et al., 1999). Data on the spatial variations have been obtained by surface-based measurements on the upwind and downwind sides of leads (Andreas et al., 1979) or on a more extensive observation grid, as in SHEBA, and by aircraft observations. The latter have most frequently been made over the ice-edge zone, with a particular interest in the effects on the ABL arising from the large thermal differences between the ice and open water (e.g., Fairall and Markson, 1987; Guest et al., 1995; Drüe and Heinemann, 2001). Studies on spatial variability have also been carried out over compact sea ice; these have mostly concentrated on cases of warm-air advection over sea ice (Bennett and Hunkins, 1986; Brümmer et al., 1994; Brümmer and Thiemann, 2002; Vihma et al., 2003), during which the spatial change is related to the gradual cooling of the air mass and the development of a stable internal boundary layer. On the other hand, the effects of cold-air advection have been studied during off-ice flows (Hein and Brown, 1988; Lüpkes and Schlünzen, 1996; Hartmann et al., 1997; Olson and Harrington, 2000, Birnbaum and Lüpkes, 2002), but in these studies the main interest has been in the development of a convective boundary layer over the open ocean or, in the case of Birnbaum and Lüpkes (2002), over a marginal sea-ice zone with a sea-ice concentration of the order of 50%.

In the previously published studies on spatial variability, both for on-ice and off-ice flows, the observations have been made in more or less stationary conditions, or the possible non-stationarity has not received particular attention. The effects of non-stationary conditions have mostly been considered in one-dimensional data analyses and theoretical studies (Overland and Guest, 1991; Guest and Davidson, 1994) as well as in idealized two-dimensional modelling studies of warm-air advection (Cheng and Vihma, 2002). Accordingly, little is known about the combined effects of spatial and temporal variations during cold-air advection. The air–ice interaction in non-stationary conditions is naturally a more challenging problem than that in stationary conditions.

In this paper, we focus on the factors generating unstable stratification over Arctic sea ice in late winter under non-stationary cold-air advection. We present aircraft observations of the near-surface fluxes and the structure of the ABL. The study case includes a combination of transient and quasi-stationary boundary-layer features. The former are generated by a large-scale cloud edge moving across the study region, and the latter by leads covering a small percentage of the surface area. After analyzing the data we present the results of a two-dimensional (2D) mesoscale model, which help one to better understand the various factors controlling the air and surface temperatures and the turbulent exchange.

2. Observations

During the Arctic Radiation and Turbulence Interaction Study (ARTIST) in March and April, 1998, the Alfred Wegener Institute for Polar and Marine Research carried out aircraft observations in the ABL over sea ice (Hartmann et al., 1999). All flights took place in the vicinity of Spitsbergen, Norway using Longyearbyen as a base. A total of 39 flight missions were carried out, that on 27 March, 1998 providing the basic data for the present study. That day Spitsbergen was located in the warm-air sector on the north-eastern side of a low-pressure system. The Polar 2 aircraft (a Dornier 228-100) flew over the sea ice to the east of Spitsbergen (Figure 1). Four horizontal legs 100 km long were flown back and forth in upwind and downwind directions (and shorter parts twice more) at an altitude of 31–54 m, with 41 m as a mean altitude (in the following, we refer to the observations on a low-level flight leg as *the 40-m air temperature*, *wind speed*, etc.). In addition, four pairs of vertical profiles were measured at the beginning and end of most of the low-level flight legs.

In the following we define the x-coordinate increasing eastwards with $x = 0$ at 23° E, where the westernmost vertical profile was flown. The flight legs were organized as follows (Table I): H1, a low-level leg from west to east;

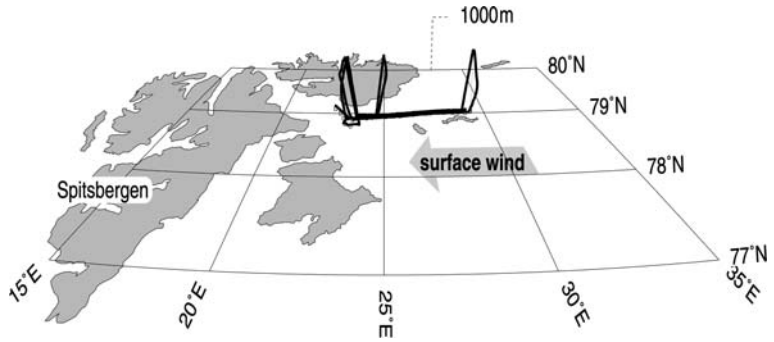

Figure 1. The flight pattern of the AWI Polar 2 aircraft over sea ice east of Spitsbergen on 27 March, 1998. Islands are marked in grey and the sea ice in white. The dotted line indicates the scale of the vertical flight legs.

H2, a low-level leg from east to west; V1, a pair of vertical profiles at the western edge of the study region at $x = 0$ km; H3, a low-level leg from west to east; V2, a pair of vertical profiles at the eastern edge at $x = 129$ km; H4, a low-level leg from east to west; V3, a pair of vertical profiles at the western edge at $x = 2$ km; H5, a short low-level leg from west to east; V4, a pair of vertical profiles at $x = 35$ km, and H6, a short low-level leg from east to west. In addition, short flight legs, not listed above, were needed for turning; these caused the small discontinuities in x in Table I. Each pair of vertical profiles consisted of a sawtooth pattern, and the data from the ascending and descending legs were averaged. Each sawtooth pattern was 11–15 km long at the base, and the x-coordinate refers to its central location.

During the flight missions, the air temperature and humidity as well as the three wind components were measured with a resolution of 120 Hz. With an average flight speed of 80 m s^{-1}, this yields a spatial resolution of 0.7 m. The temperature sensors have an accuracy of ± 0.25 K for the absolute value. The upward and downward shortwave and longwave radiation streams were

TABLE I

Mean observation times and locations of the primary flight legs.

	Flight leg									
	H1	H2	V1	H3	V2	H4	V3	H5	V4	H6
UTC time	1159	1229	1247	1309	1329	1346	1404	1412	1419	1430
x-Coordinate (km)	24 → 119	22 ← 111	0	11 → 119	129	19 ← 126	2	1 → 29	35	29 ← −28

The vertical profile flights are indicated by V1–V4 and the horizontal low-level flight legs by H1–H4. The x-coordinate increases eastwards and is defined as zero at 23° E.

observed with a resolution of 12 Hz, corresponding to a spatial resolution of 7 m. The errors in the measurements of the radiative fluxes are 1% in linearity and cosine behaviour (Freese, 1999). The surface temperature as well as the sea-ice concentration were derived from the radiation data obtained using a Heimann KT4 radiation thermometer, which is sensitive in the range of 8–14 μm. The opening angle is 0.6°, corresponding to a ratio of distance to field diameter of 100:1. The accuracy of the surface temperature data is within 1 K. Details of the aircraft, its instrumentation and the measurement accuracies are described in Kottmeier (1996).

The turbulent fluxes of momentum, sensible heat and latent heat were calculated from the instantaneous observations applying a lowpass filter, corresponding to a running mean over some 20 km. For comparison, the fluxes were also calculated by integrating over the cospectra for the range from 1 m to 20 km. Integrated over the whole study region, the two methods yielded the same results, and we present those based on the lowpass filter. It should be noted that the aircraft data of turbulent fluxes do not necessarily represent the true surface fluxes, since the constant-flux layer often, and especially under stable stratification, does not reach the flight altitude of approximately 40 m. We will take this into account in the model comparisons.

In the west the ice field was compact, but in the east there was a region almost 30 km wide with small leads covering 5% of the surface area. Most of the leads were not open but covered by thin ice with a surface temperature ranging from approximately −6 to −2 °C. High-resolution data of the surface temperature in the lead region are shown in Figure 2. Easterly winds had prevailed for a few days and the ice was packed against the east coast of Spitsbergen, so that the ice surface was therefore relatively rough, with pressure ridges, especially in the eastern part of the study region. The air mass had a long fetch (of at least 1000 km) over the sea ice.

3. Data Analyses

The vertical profiles of the potential temperature and wind speed are shown in Figure 3. We see a large difference in the ABL height and mixed-layer temperature between the upstream region (V2, $x = 129$ km) and the downstream region (V1 and V3, $x = 0$–2 km). In addition, the ABL becomes colder and shallower during the time interval of 77 min between the two measurements, V1 and V3, in the downstream region. At $x = 35$ km, another 15 min later (V4), the ABL is colder and shallower still.

Data from the four longer low-level legs, H1–H4, in the region $x = 11$–126 km are shown in Figures 4 and 5 as 2-km averages. The 40-m potential temperature decreases roughly linearly from west to east, while the surface

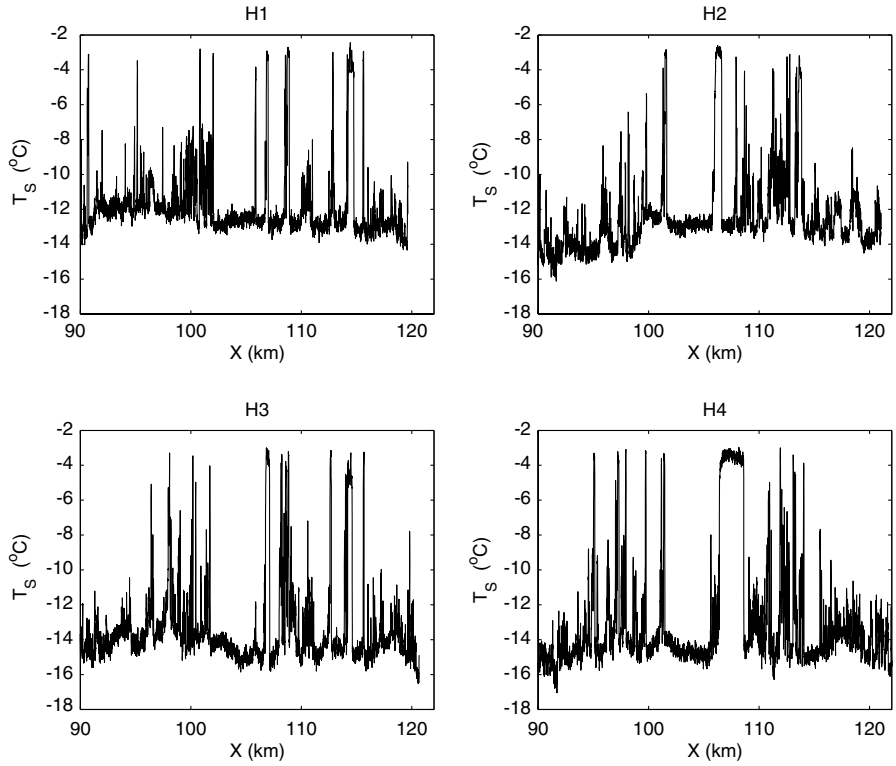

Figure 2. Surface temperature in the lead region observed with a 7-m spatial resolution during the four low-level flight legs H1–H4.

temperature has its minimum in the middle of the study region, where the surface is slightly colder than the air (Figure 4a). The surface temperature peak in the east is related to the existence of leads in this region. The sensible heat flux is directed upwards over most of the study region, reaching its maximum values in the eastern part. The wind speed and momentum flux reach their minimum values at $x = 60$–70 km, with their patterns somewhat resembling the surface temperature field. The atmospheric pressure increases almost linearly from west to east. During the first low-level leg, the pressure in the eastern part was up to 0.8 hPa lower than during the successive flight legs (Figure 5b).

From the point of view of radiative fluxes (Figure 5c and d), the study region can be roughly divided into three sub-areas, i.e., the cloudy western part ($x < 30$–75 km), the clear middle part (70 km $< x <$ 100 km), and the eastern part with thin clouds ($x >$ 100 km). The locations of the sub-areas are approximate, due to the non-stationary situation. The downward shortwave radiation flux had its maximum values in the cloud-free region, while the downward longwave radiation flux was approximately 240 W m^{-2}

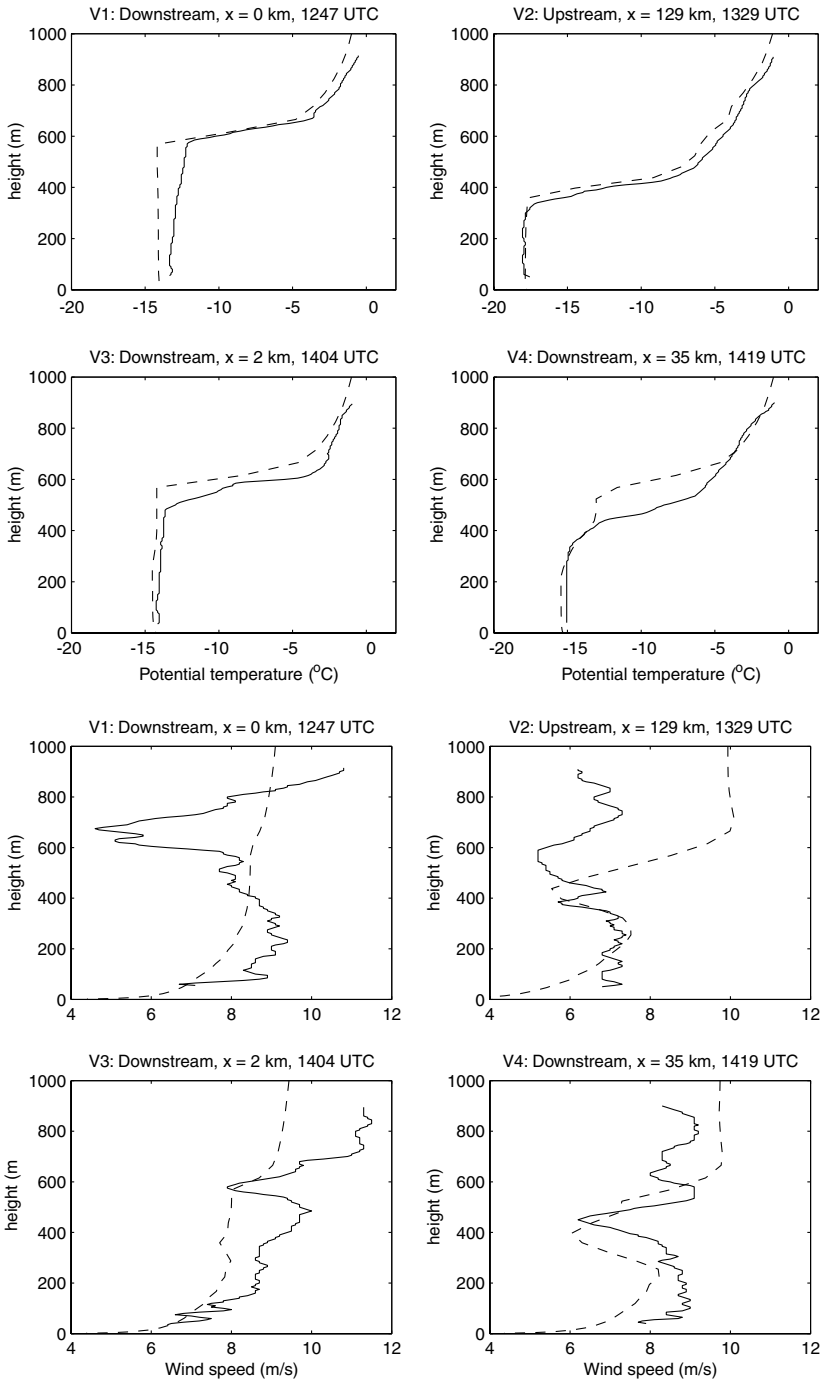

Figure 3. Observed (continuous lines) and modelled (dashed lines) vertical profiles of air potential temperature and wind speed.

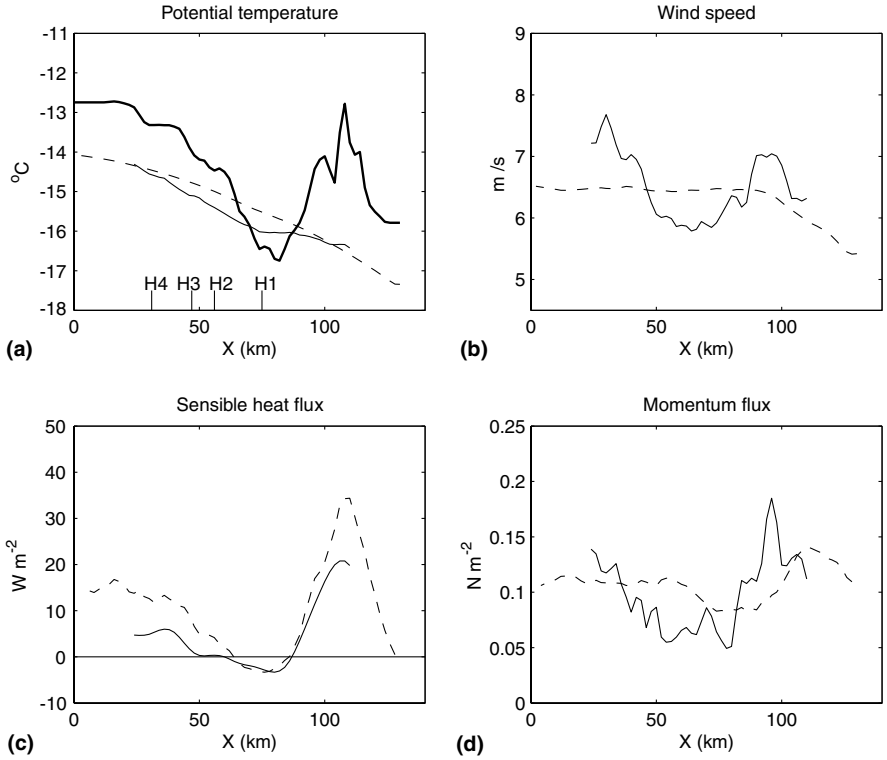

Figure 4. Observed (continuous lines) and modelled (dashed lines) horizontal profiles of the surface (thick line) and air potential temperature, wind speed, and the turbulent fluxes of sensible heat and momentum averaged over the four flight legs, H1–H4, at a height of 40 m. Each leg lasted for 30 min, centred at the times indicated in Table I. The vertical bars in panel (a) indicate the location of the primary cloud edge during H1–H4.

below the thick cloud cover in the west, and its minimum of 170–180 W m^{-2} at $x = 80$–90 km roughly collocated with the surface temperature minimum. The location of the primary edge of the thick cloud cover was detected on the basis of the downward longwave radiation flux values (Figure 5d; some 10 km east of the primary cloud edge there was also a narrow cloud region). The time series of the location is shown in Figure 6a, which indicates a westward advection of clouds at an almost constant speed of 7.3 m s^{-1}. The vertical profiles of the upward and downward longwave radiation fluxes are shown in Figure 7. The cloud tops are distinguishable approximately at heights of 600, 300, 550, and 400 m in V1, V2, V3, and V4, respectively. In the case of profile V1, with a thick, distinct cloud top, the longwave net radiative flux divergence calculated for the uppermost 50-m cloud layer corresponds to a radiative cooling rate of 80–90 K day^{-1}. There was horizontal heterogeneity in the cloud cover, which affected especially the shortwave fluxes; for this reason, their vertical profiles are not shown.

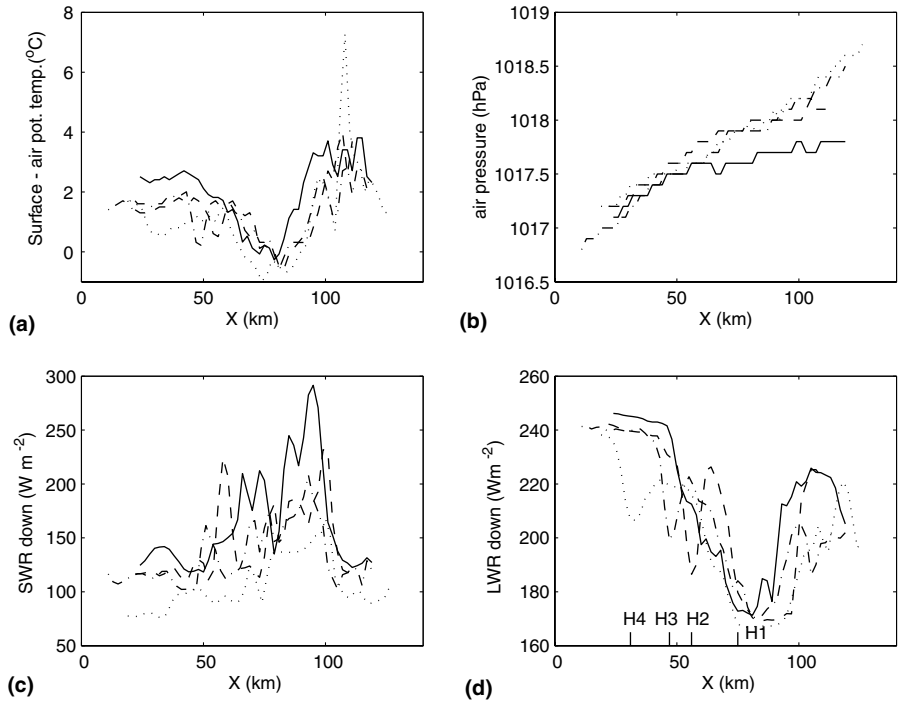

Figure 5. Observed horizontal profiles of (a) surface–air potential temperature difference, (b) atmospheric pressure, (c) incoming shortwave radiation flux and (d) incoming longwave radiation flux, as measured during the low-level flight legs: leg 1 (continuous line), leg 2 (dashed line), leg 3 (dot-dashed line), and leg 4 (dotted line). The vertical bars in panel (d) indicate the location of the primary cloud edge during H1–H4.

Next we aim at understanding the contribution of the various terms in the heat budget of the ABL and, in particular, at determining the Eulerian change of potential temperature, which is later needed for our model application (see Section 5.1). Assuming a well-mixed ABL, no water phase changes, no vertical advection, and cross-flow homogeneity $\partial/\partial y = 0$, we can approximate the Lagrangian change in potential temperature as a result of two terms: turbulent heat flux convergence and radiative flux convergence:

$$\frac{d\Theta_{\mathrm{ABL}}}{dt} = \frac{\partial \Theta_{\mathrm{ABL}}}{\partial t} + u_{\mathrm{ABL}} \frac{\partial \Theta_{\mathrm{ABL}}}{\partial x} = -\frac{1}{\rho c_p} \frac{\partial H}{\partial z} - \frac{1}{\rho c_p} \frac{\partial Q_{\mathrm{Rad}}}{\partial z}, \tag{1}$$

where the subscript ABL refers to a mean value in the layer from 40 to 300 m. Q_{Rad} is the net radiative flux (shortwave + longwave) defined positive upwards similarly to the turbulent heat flux H; u is the eastward wind component ($u < 0$), ρ is the air density, and c_p is the specific heat. Unfortunately we had flux data from a single level only, but the area-average of the turbulent flux convergence term was estimated by assuming that H decreases

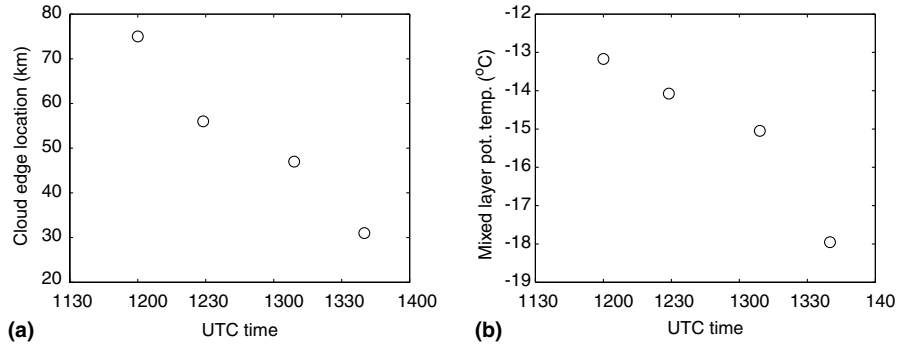

Figure 6. Results of the analyses of the spatio-temporal development of the ABL: (a) time series of the location of the primary cloud edge and (b) mixed-layer potential temperature as a function of the time of the air-mass arrival at $x = 0$ km.

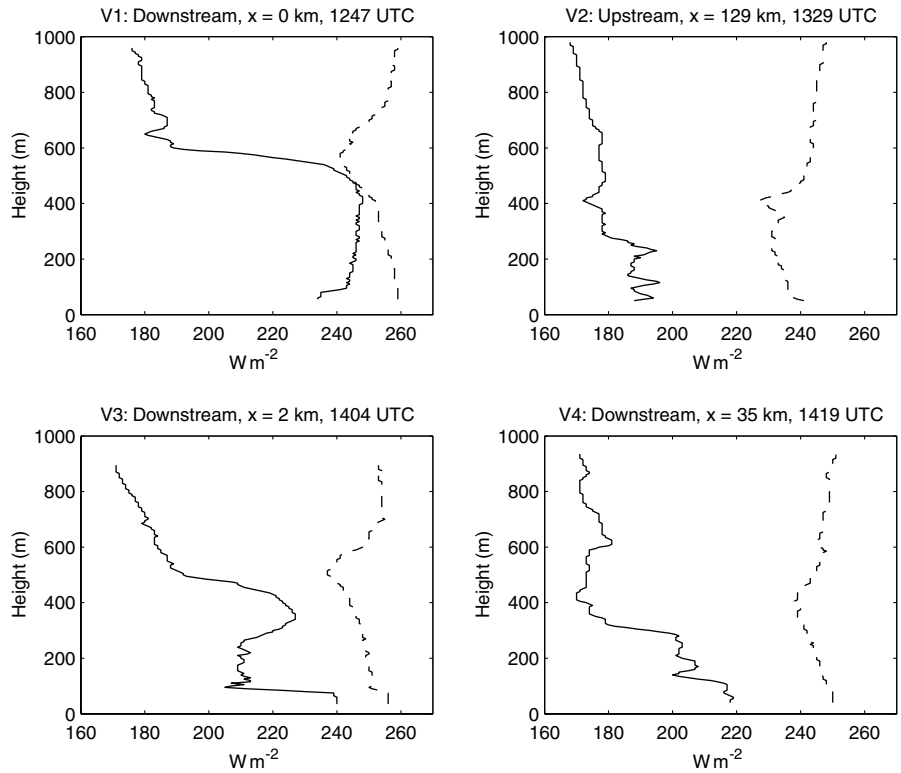

Figure 7. Vertical profiles of the downward (solid line) and upward (dashed line) longwave radiation fluxes as measured during the profile flights V1–V4.

linearly to zero between the surface and the ABL top (Table II, area-averages for the layer 30–400 m). The radiative heating term was calculated on the

TABLE II
Heat budget of the ABL.

Region	Layer	$d\theta/dt$	$\partial\theta/\partial t$	$u\ \partial\theta/\partial x$	$-(1/\rho c_p)\ \partial H/\partial z$	$-(1/\rho c_p)\ \partial Q_{\mathrm{Rad}}/\partial z$
Area-average	40–300 m	0.41	−1.94	2.35	0.15	0.26
Area-average	40-m level	0.30	−1.12	1.42	0.15	0.15
Inflow boundary	40–300 m	0.09	−2.23	2.33	0.10	−0.01
Inflow boundary	40-m level	0.18	−1.76	1.94	0.10	0.08

Values are in 10^{-4} K s^{-1}.

basis of observed data from V1 to V4, and $d\theta_{\mathrm{ABL}}/dt$ as the sum of the radiative and turbulence terms (Table II).

To distinguish between the Eulerian change and advection in (1), we estimated the time of arrival at $x = 0$ for the air masses observed by each profile flight V1–V4. This was made assuming that the wind speed remained the same as observed until the air mass reached $x = 0$. The $\theta_{\mathrm{ABL}}(x = 0)$ was calculated on the basis of the observations, the estimated travel time to $x = 0$, and the $d\theta_{\mathrm{ABL}}/dt$ given in Table II. The results are shown as a function of the calculated time of arrival at $x = 0$ km (Figure 6b). Obviously, the decrease of θ_{ABL} at $x = 0$ was almost linear, and yielded an estimate for the Eulerian change $\partial\theta_{\mathrm{ABL}}/\partial t$. Using it in Equation (1), we could also estimate the advection term. The results for both $\partial\theta_{\mathrm{ABL}}/\partial t$ and $u_{\mathrm{ABL}}\partial\theta_{\mathrm{ABL}}/\partial x$ are shown in Table II.

For the height of 40 m, it was possible to calculate the Eulerian and Lagrangian changes in air potential temperature ($\theta_{40\ \mathrm{m}}$), as well as the advection term, directly on the basis of the data from the four low-level flight legs, without any assumptions about the factors affecting the heat budget. The radiative heat flux convergence at a height of 40 m was solved as a residual from (1). The results are shown in Table II.

The above-mentioned analyses were based on spatially averaged data from the whole study region, but we are aware that the diabatic heating terms showed spatial variations. To obtain proper inflow boundary conditions for the mesoscale model, we made separate analyses concentrating solely on the inflow region. It should be noted that there were no leads actually at the inflow boundary ($x = 130$ km) but only some 15 km downwind of it (Figure 4a). The analyses were based on radiative flux data from profile V2, heat flux data from the low-level legs, and the observed $\partial\theta_{40\mathrm{m}}/\partial t$ in the inflow region. The calculation method was otherwise similar to that for the spatially averaged data, and $\partial\theta/\partial x$ over the whole study region had to be applied. The results are shown in Table II. There was warm-air advection above the mixed layer, since, with the decreasing boundary-layer height, the upper mixed layer

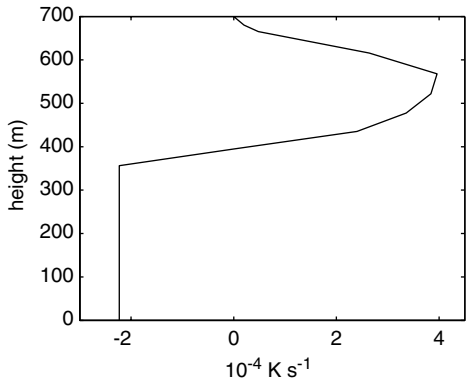

Figure 8. $\partial\theta(z)/\partial t$ at the inflow boundary ($x = 129$ km) as estimated on the basis of the aircraft observations.

air at a height of 300–600 m was replaced by warmer inversion-layer air flowing from the east (Figure 3). The resulting $\partial\theta(z)/\partial t$ is shown in Figure 8. The inflow boundary conditions for air specific humidity (q) were calculated analogously to those for the potential temperature; the resulting $\partial q/\partial t$ was -2.5×10^{-8} s^{-1} (almost constant with height).

To sum up, the data allowed us to estimate the heat budget for the ABL (height range 40–300 m) and for the level of 40 m almost independently of each other. Only the result for the turbulent heat flux convergence was based on the same data (the flux convergence was assumed constant in height). Considering the area-averages, the analyses both for the height of 40 m and for the 40–300 m layer suggested that 80% of the Eulerian change in time was explained by cold-air advection and 20% by diabatic heating (Table II). At the inflow boundary with no leads and only a thin cloud cover the situation was, however, almost adiabatic.

4. Numerical Model

The main objective of the model simulations is to give a better understanding of the factors responsible for the spatial and temporal variations in the observed ABL structure and the direction and magnitude of the sensible heat flux. The cloud cover, leads, and the cold-air advection may all have contributed to the generation of the well-mixed boundary layer. Our attention is therefore focused on the modelling of these three effects. Furthermore, we study the steady-state ABL height and mixed-layer temperature under clear and overcast skies.

4.1. General description

The numerical model used is a University of Helsinki two-dimensional hydrostatic boundary-layer model. The model has 92 points in the horizontal and 50 in the vertical; the vertical coordinate is a terrain-following modified σ; $\sigma = (p - p_t)/(p_s - p_t)$, where p is pressure, and subscripts s and t refer to the surface and model top, respectively. The horizontal grid length is 2 km and the time step accordingly 4 s. The vertical grid has quasi-logarithmic spacing with the lowest levels at approximately 1.5, 4, 8, 15, and 24 m. The upper boundary conditions are applied at 3 km, where the wind becomes geostrophic. The mesoscale flow is forced by a large-scale pressure gradient represented by the geostrophic wind. All fluxes vanish at the model top, and zero-gradient conditions are applied at the lateral boundaries. Vertical diffusion (mixing length closure) is solved by an implicit method, and instead of explicit horizontal diffusion, a weak lowpass filter is applied to all fields.

The equations of the model dry dynamics are as given in Alestalo and Savijärvi (1985), but the physical parameterizations are as in Savijärvi (1997) with humidity, clouds, and an advanced radiation scheme included. The model has previously been used in several mesoscale studies, including studies over sea-ice margins (Vihma and Kottmeier, 2000; Vihma and Brümmer, 2002; and Vihma et al., 2003). Savijärvi (1991) validated the model against an extensive boundary-layer dataset in both convective and stable conditions, and Savijärvi and Kauhanen (2001) and Savijärvi and Amnell (2001) produced comparisons with measurements over snow and boreal forest.

4.2. Turbulence and radiation schemes

The vertical diffusion coefficient K depends on the local wind shear and on the local Richardson number Ri:

$$K = l^2(dU/dz)f(Ri), \tag{2}$$

where the mixing length is given by $l = \kappa z/(1 + \kappa z/\lambda)$ with λ as its asymptotic maximum value (we use $\lambda = 50$ m; for a discussion of this value see Vihma et al., 2003) and κ as the von Karman constant (set to 0.4). In conditions of stable stratification, the following stability function is used for momentum, heat, and moisture:

$$f(Ri) = \begin{cases} \max\left[b, (1 - 5Ri)^2\right] & \text{for} \quad 0 \leq Ri < 0.2, \\ b & \text{for} \quad Ri \geq 0.2. \end{cases} \tag{3}$$

The parameter b represents the background turbulence in very stable conditions, and prevents K from decreasing to zero. On the basis of Vihma et al. (2003), we set $b = 0.005$. In the case of unstable stratification,

$f(Ri) = (1-16Ri)^{1/2}$ for momentum and $f(Ri) = (1-64Ri)^{1/2}$ for heat and moisture.

The longwave radiation is calculated using a six-band emissivity scheme, which is based on the well-tested code of the European Centre for Medium-Range Weather Forecasts model (Morcrette, 1991) but further improved (Savijärvi and Räisänen, 1998) to also allow good accuracy with the high vertical resolution of our mesoscale model. The scheme assumes that clouds are of mixed-phase with the portions of liquid water and ice depending on the temperature. The radius of cloud droplets is set to 10 μm and that of ice crystals to 50 μm; cloud droplets dominate the thermal radiative transfer in the present temperatures. The shortwave radiation is calculated with a four-band two-stream scheme (Savijärvi et al., 1997). To save computer time, the full radiative transfer is solved every 180 s.

4.3. Surface temperature and flux schemes

In the reference simulation we use prescribed surface temperatures from observations, but we also make sensitivity tests with the surface temperature modelled with an eight-layer scheme for the heat conduction in the snow and ice. We do not have data on the ice and snow thickness (h_i and h_S, respectively), but on the basis of the submarine data of Bourke and Garrett (1986), we apply 1.0 m for h_i and 0.1 m for h_S. With such relatively large values, the conductive heat flux is fortunately not too sensitive to h_i and h_S (Makshtas, 1991). For the thermal conductivities in snow and ice we use 0.25 and 2.1 W m^{-1} K^{-1}, respectively (there is some uncertainty in the former (Sturm et al., 2002)). The surface of each grid interval is divided into sub-sections of snow-covered ice and leads on the basis of the observations. The grid-averaged surface fluxes of heat and moisture are then calculated as area-averages of the local fluxes applying the (basic) mosaic method (Vihma, 1995).

We prescribe the momentum roughness length z_0 on the basis of the observed momentum flux τ,

$$\tau_z = -\rho C_{\mathrm{D}z} V_z^2, \tag{4}$$

$$C_{\mathrm{D}z} = \frac{k^2}{(\log(z/z_0) - \psi_\mathrm{M}(z/L))^2}, \tag{5}$$

where L is the Obukhov length and ψ_M is the stability function for momentum. Calculating the drag coefficient $C_{\mathrm{D}z}$, and further z_0, directly from (4) to (5) would, however, result in an underestimation of the surface roughness, because it is assumed in (4) that the constant-flux layer extends up to the measurement level z of the momentum flux and wind speed. We therefore apply (4) to calculate C_{D40m} directly from the observations, and

then apply the equation of Garbrecht et al. (2002, their Equation (13)) to calculate C_{D10m} from C_{D40m}:

$$C_{\mathrm{D10\,m}} = C_{\mathrm{D}z}\left[a + \left(\frac{1-a}{10}\right)z\right], \tag{6}$$

where $a = 0.174\,L^{1/4}$ and in (slightly) unstable conditions, with $L < 0$, a near-neutral approximation of $L = 250$ m is used. Then $z_0(x)$ results from (5) assuming that the constant-flux layer extends up to 10 m. We calculate the thermal roughness length $z_{\mathrm{T}}(x)$ over ice according to Andreas (1987). The data from the low-level flight legs H1–H4 are averaged to calculate $z_0(x)$ and $z_{\mathrm{T}}(x)$.

5. Reference Run

5.1. Initial and boundary conditions

The model domain covered the region $x = 0$–130 km, with the inflow boundary at 130 km. With the mean ABL wind speed of 8.6 m s^{-1} (as observed at V1: $x = 0$ km at 1247 UTC), it had taken 4.2 h for the air mass to travel from $x = 130$ to 0 km, and the simulations were accordingly started at 0835 UTC.

We studied the possibility of prescribing the inflow boundary conditions on the basis of NCEP/NCAR (National Centers for Environmental Prediction/National Center for Atmospheric Research) reanalyses and the operational analyses of the regional model HIRLAM, but found that the potential temperature profiles differed so much from the aircraft observations that these low-resolution analyses could be of no use for detailed modelling of mesoscale processes. Hence, we set the inflow boundary conditions on the basis of the data analyses in Section 3. The initial inflow $\theta(z)$ was calculated from the $\theta(z)$ observed at V1 taking into account the area-averaged $d\theta/dt$ (Table II) that had acted on the air mass during its traverse from $x = 130$ to 0 km. A 24-h spin-up run was then made with a one-dimensional model version to initialize the inflow $\theta(z)$ for the 2D model. During the actual simulation, we applied the $\partial\theta(z)/\partial t$ shown in Figure 8. For air specific humidity, an inflow $\partial q/\partial t$ of -2.5×10^{-8} s^{-1} was applied. In the subsequent sensitivity tests, the thermodynamic snow/ice model was initialized by running it into a steady state for the atmospheric forcing at 0835 UTC.

The geostrophic wind components (u_{G} and v_{G}) were set according to the large-scale pressure gradient and the aircraft observations above the boundary layer viz.: $u_{\mathrm{G}} = -8.0$ m s^{-1}, $v_{\mathrm{G}} = 5.4$ m s^{-1}. The initial wind profile was calculated according to the Ekman–Taylor spiral, and zero-gradient boundary conditions were applied during the time integration.

The cloud condensate content was unfortunately not measured, but is needed as an input for the radiation scheme. Hence, to produce vertical and

horizontal radiative flux profiles in agreement with the observed ones, we prescribed the initial (0835 UTC) cloud cover in the whole model domain as having a cloud condensate content of 30 g m^{-2} (mixed-phase) integrated from $z = 500$ to 600 m. The cloud edge was advected westwards with the modelled wind velocity. In addition to the retreating thick cloud, thin cloud (8 g m^{-2} integrated from $z = 250$ to 350 m) was prescribed in the region $x >$ 90 km (based on the radiative fluxes and visual observations). We prescribed the surface potential temperature $\theta_S(x, t)$ according to the observations from the low-level flight legs. By prescribing $\theta_S(x, t)$ we are able to study the quality of the model results with respect to the ABL evolution without introducing additional inaccuracy caused by the bias in $\theta_S(x, t)$. In the sensitivity tests we will, however, also simulate $\theta_S(x, t)$.

5.2. Results

The results of the reference run are shown in Figures 3, 4, and 9. Cross-sections of the potential temperature at the times of the vertical profile flights

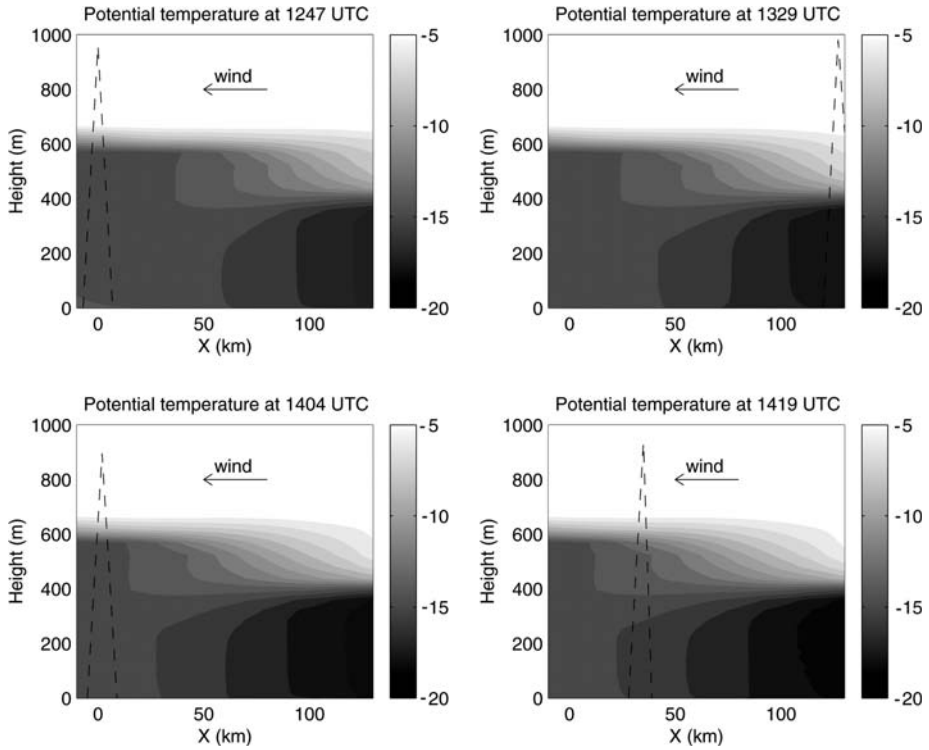

Figure 9. Modelled cross-sections of the potential temperature at the times of the vertical profile flights (marked by dashed lines).

are shown in Figure 9 to illustrate the overall evolution of the case: cold air in a shallow boundary layer is advancing from the eastern inflow region (large x), but above the boundary layer there is warm-air advection. The vertical profiles of wind speed show that at V1 the model result is more constant with height than observed, but at V2 and V4 the agreement is very good (Figure 3). In all profiles observed, the wind speed decreases with height just above the mixed layer but then increases again further above. Also the vertical profiles of potential temperature are well reproduced, although the mixed layer is 0.8–1.9 K too cold at V1, and part of the inversion layer is too high at V4.

In the following comparisons of model results with the observations on the low-level flights, the model results are interpolated to the true observation height at each horizontal location. Both observations and model results are averaged over the four low-level flight legs. With $\theta_S(x)$ and the inflow $\partial\theta/\partial t$ prescribed, the $\theta_{40m}(x)$ increases with fetch at the same mean rate as observed (Figure 4). In the middle of the study region, the modelled θ_{40m} is, however, slightly higher than observed; there is no obvious reason for this, but even though the wind direction coincided with the flight track (i.e., the model domain) to within $\pm 10°$, there may be some influences from the orthogonal directions. The order of magnitude of the wind speed and momentum flux is well reproduced by the model, but the horizontal variations in the wind speed are poorly reproduced. The good results for the momentum flux demonstrate that Equation (6) (Garbrecht et al., 2002) also works well under neutral and weakly unstable conditions. It was developed and previously validated mostly for stable stratification.

The modelled sensible heat fluxes shown in Figure 4 (and later) are grid-averages for the 2-km grid spacing of the model. The largest local fluxes over leads, calculated applying the mosaic method, reached 140 W m^{-2}. In the eastern part of the study region, the air is colder than the surface, and H is upwards. There, the mean lead fraction was 5% and only thin clouds were present during the period of the comparisons shown in Figure 4. In the region $x \approx 60$–80 km, the air is warmer than the surface, and H is accordingly downwards. A region of unstable stratification is again found when $x < 50$ km. There the ice concentration was 100%, but the cloud cover was thick. The modelled spatial variations in H agree reasonably well with the data, although the model overestimates the upward fluxes.

6. Sensitivity Tests

The fair agreement between the observations and the reference run demonstrated that the assumptions made in the data analyses of Section 3 were supported by the mesoscale model simulations. In particular, the method of

estimating the initial inflow $\theta(z)$ and its evolution proved successful. The situation was nearly adiabatic, and the space–time variations of the boundary-layer height and temperature were mostly controlled by the cold-air advection and the retreat of the cloud cover. The reference run alone did not, however, reveal the physical reasons for the spatial variations in the thermal stratification of the surface layer. The effects of the leads and clouds can be suspected on the basis of Figure 4. To study them in more detail we applied the model in the following sensitivity tests:

S1. Prescribed cloud cover was as in the reference run, but the surface temperature was modelled with leads included. The eight-layer scheme was applied for the calculation of the surface temperature of thick ice. The lead fraction f was set according to the high-resolution surface temperature data (Figure 2; the frequency of occurrence of cases with $T_s > -6$ °C was averaged over the four horizontal flight legs). In the grid cells from 90 to 117 km f varied from 1% to 5%, except for one grid cell in which f was 30%. Elsewhere f was 0%. The lead surface temperature was prescribed as −3.4 °C, which represented the thin-ice peak in the high-resolution T_s distribution. The grid-averaged surface sensible heat flux from grid cells with $f > 0$ was calculated applying the mosaic method.

S2. Cloud cover was prescribed and the surface temperature was modelled, but no leads were included.

S3. As S1, but with no clouds in the model.

S4. As S2, but no clouds included.

With respect to $\partial\theta(z)/\partial t$ at the inflow boundary, sensitivity tests S1–S4 were similar to the reference run. In addition, we carried out sensitivity test S5, which was the same as S1 but instead of the prescribed $\partial\theta(z)/\partial t$ at the inflow boundary, zero-gradient boundary conditions were applied. Accordingly, there was no large-scale cold-air advection into the model domain.

The results of the sensitivity tests are shown in Figures 10–12. We first look at the horizontal distributions of the surface and 40-m potential temperatures and the sensible heat flux. In S1, with the prescribed clouds and θ_S modelled with leads included, the results (Figure 10) are very close to those of the reference run (Figure 4), which demonstrates that the eight-layer scheme reproduced well the snow and ice thermodynamics (additional simulations applying a force-restore scheme yielded worse results). The sensible heat flux is overestimated in the lead region, as is also the air temperature in the middle of the study region, but otherwise the horizontal distributions are well reproduced. The success of S1 and the reference run is naturally partly based on the tuning of the cloud condensate content so that the modelled radiative fluxes matched those observed (Section 5.1). However, we use the same cloud

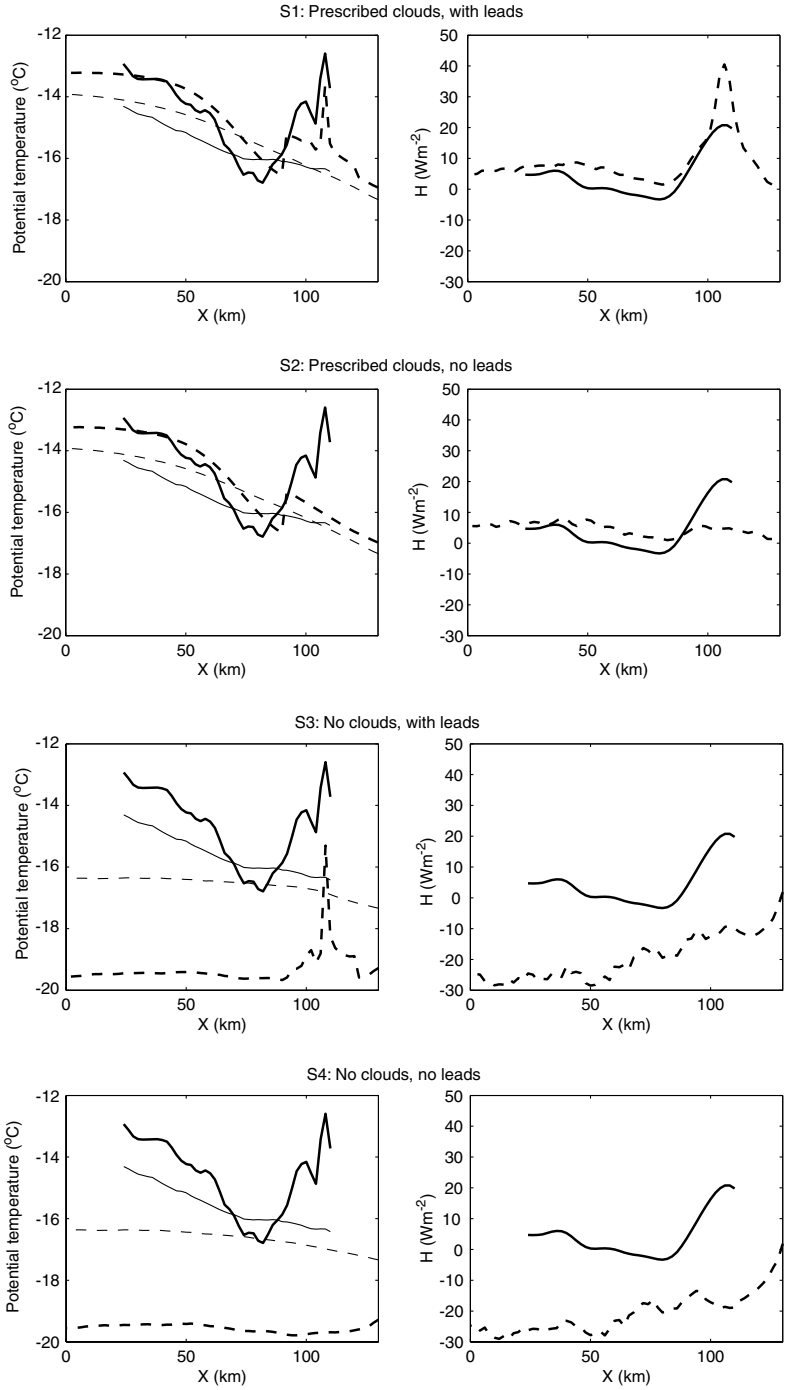

Figure 10. Observed (continuous lines) and modelled (dashed lines) horizontal distributions of the potential temperature of the surface (thick lines) and air (thin lines) and the sensible heat flux averaged over the four low-level flight legs for the sensitivity tests S1–S4.

condensate content in all the model runs with clouds included, and we therefore trust that our approach yields reliable results on the relative importance of clouds, leads, and advection.

In S2, with the prescribed clouds but without leads, the surface temperatures are too cold in the lead region, and the sensible heat flux does not show any peak there. In S3, with leads but without clouds, θ_S is far too low, resulting in a downward sensible heat flux. In the individual grid cell with $f = 30\%$ ($x = 108$ km), θ_S exceeds θ_{40m} resulting in an upward grid-averaged H at the surface, but the upward flux does not reach a height of 40 m. In S4, with no clouds and no leads, the situation is almost the same as in S3, except for the surface temperature peak. On the basis of the results of S1–S4, it appears that, under cold-air advection conditions, the thick clouds were responsible for the upward sensible heat flux in the downwind region, while leads together with the thin cloud caused the upward flux in the upwind region. The effects of leads and clouds interact non-linearly with the ABL turbulence and advection: in the presence of clouds, the effect on the ABL of the leads appears stronger than in the absence of clouds (Figure 10). This is because, in the absence of clouds, the stratification is so stable that the upward surface heat flux from the leads does not penetrate to any great height. Consequently, air in the lowest few metres is heated, but heat is then transferred to the ice immediately downwind of the leads. On the other hand, in such conditions the lead effect on the ice and snow thermodynamics (transmitted via the atmospheric surface layer) is larger.

To understand the importance of the imposed cold-air advection, we consider the model results without cold-air advection (S5, Figure 11). $\theta_S(x)$ is greater than in S1, and $\theta_{40m}(x)$ is much larger and it is constant downstream. The sensible heat flux displays only a weak positive peak in the upwind region. The results, accordingly, suggest that the observed upward sensible heat flux is a combined effect of clouds, leads, and cold-air advection.

Besides the effects on the near-surface conditions, the sensitivity tests without clouds (S3 and S4) revealed effects on the mixed layer and the ABL top (Figure 12). Without the presence of the cloud cover, the stratification was slightly stable right from the surface, and $\theta(z)$ had a smoother shape without a well-defined ABL top. The latter seems to be due to the lack of cloud-top radiative cooling. At V2 ($x = 129$ km) a mixed layer with a distinct ABL top is also seen in the model results, but this is due to the location of V2 at the inflow boundary. The model results for $\theta(z)$ with and without leads (S3 and S4) were practically identical: the maximum difference was 0.04 K (the results without leads are therefore not shown in Figure 12). The profiles V1, V3, and V4 are located 90–55 km downwind of the lead region, and the heat originating from the leads had been distributed through such a large air volume in the mixed layer that the temperature increase at any given level was small. A local H of

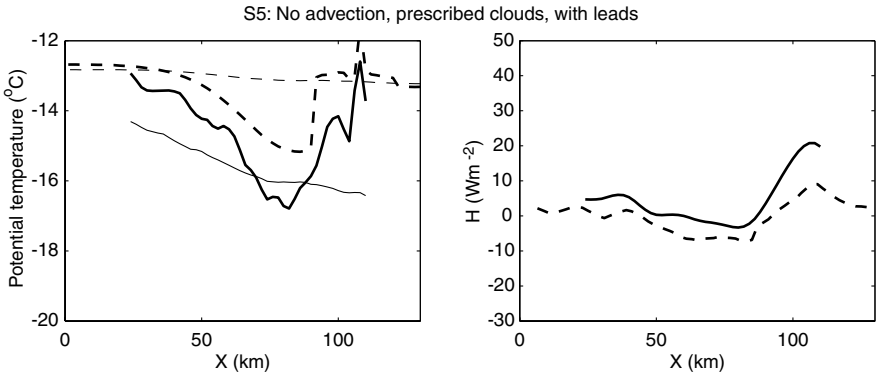

Figure 11. As Figure 10, but for sensitivity test S5 without the effect of cold-air advection.

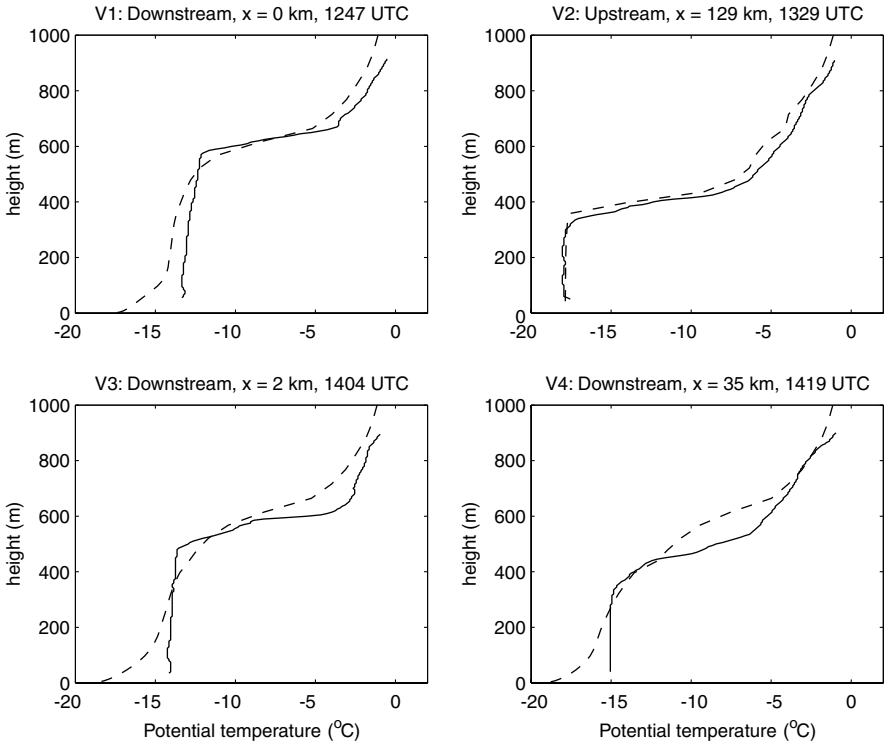

Figure 12. Observed (continuous lines) and modelled (dashed lines) profiles of potential temperature in the sensitivity test S3.

140 W m^{-2} over leads, from a region 30 km wide with a mean lead fraction of 5%, only produces a temperature increase of 0.04 K when the heat is distributed through a 600-m-deep well-mixed layer.

7. Steady-State Simulations

To better understand the formation of a well-mixed cloudy ABL, we made the following quasi-steady-state simulation. The initial $\theta(z)$ was set so that the inversion base was at 300 m, as observed in V2 under clear skies, and the inversion strength as observed in V1 under overcast skies (Figure 13). The initial cloud condensate content was set as in the reference run (30 g m^{-2} from $z = 500$ to 600 m), but the cloud was now prescribed to be constant. The geostrophic forcing and the initial humidity and wind profiles were as in the reference run. The surface temperature was modelled with the eight-layer scheme, with leads included. The model was integrated for five days with zero-gradient boundary conditions for the wind, air temperature, and air humidity. Two runs were made: one with the background turbulence parameter $b = 0.005$, as in the reference run, and the other with $b = 0.1$ (see Equation (3)).

The resulting quasi-steady-state potential temperature profiles are shown in Figure 13. We see that the cloud top indeed controls the inversion base height, but in the run with $b = 0.005$ there are two separate mixed layers: a lower one due to surface-based mixing and an upper one due to cloud-top radiative cooling. Such a layered structure is common in the Arctic but not observed in this case. With $b = 0.1$, two mixed layers are first formed, but more mixing now takes place in the inversion layer between them, and eventually the mixed layers merge. The shape of the steady-state $\theta(z)$ is closer to the observed profile under cloudy skies.

Here the results are better with $b = 0.1$, allowing more background turbulence in the inversion layer, although in the clear-sky simulations in Vihma et al. (2003) $b = 0.005$ was a better choice. The surface heterogeneity (leads,

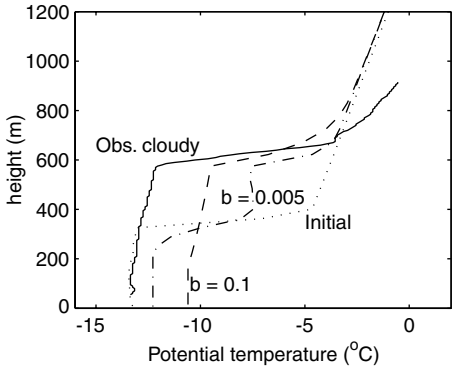

Figure 13. Observed potential temperature profile at V1 (solid line), as well as initial (dotted line) and steady-state (with $b = 0.1$ as dashed line; $b = 0.005$ as dot-dashed line) profiles for a 120-h simulation under overcast skies.

regions of rougher ice) may have increased the available background turbulence. Our results are close to those of Wang et al. (2001), and their experiments with a single cloud layer also demonstrated the formation of two separate mixed layers, which gradually merged. The main effect was a cooling of the ABL, although close to the surface there was a 1–2 K warming; these fit well our results with $b = 0.1$ (Figure 13).

8. Conclusions

Aircraft observations of the ABL over Arctic sea ice were made in March during non-stationary conditions of easterly cold-air advection with a cloud edge retreating through the study region. The sea-ice concentration and roughness varied in space. The surface-layer stratification was unstable in the eastern and western parts of the study region, but stable in the central region. Analyses of the ABL heat budget suggested that 80% of the Eulerian change in time was explained by cold-air advection and 20% by diabatic heating. Although only one vertical profile was measured at the inflow boundary, the heat budget analysis made it possible to construct the relevant time-dependent inflow boundary conditions for a two-dimensional mesoscale model. With the cloud cover and inflow potential temperature profile prescribed as a function of time, the case was well simulated.

Previous studies, e.g., Persson et al. (2002), have documented that the ABL stratification over Arctic sea ice can be slightly unstable even in winter, and the effects of various individual factors in generating the unstable stratification have been addressed (see Section 1). The effects of several factors acting simultaneously have so far received little attention. Our model sensitivity tests demonstrate that, from the point of view of surface-layer stratification, the important factors include downward longwave radiation from clouds, upward heat fluxes from leads, and cold-air advection. In our case, the upward sensible heat flux was generated by the combined effect of thick clouds and cold-air advection in the western parts, and by thin clouds, leads, and cold-air advection in the eastern parts. These factors interacted nonlinearly with each other. From the point of view of the ABL temperatures, the lead effect was far less important than the cloud effect. The latter shaped the temperature profile via cloud-top radiative cooling (generating a top-down mixing) and radiative heating of the snow surface (generating a turbulent surface flux).

Five-day simulations demonstrated that, under overcast skies, the evolution towards a deep, well-mixed ABL may take place via a formation of two mixed layers: one related to mostly shear-driven surface mixing and the other to buoyancy-driven top-down mixing due to the cloud-top radiative cooling. These mixed layers may gradually merge.

Acknowledgements

We are grateful to Lars Kaleschke, University of Bremen, for providing information on the large-scale ice cover. Our introduction includes comparisons based on observations by the SHEBA Atmospheric Surface Flux Group, Ed Andreas, Chris Fairall, Peter Guest, and Ola Persson. This study was supported by the German Bundesministerium für Bildung und Forschung (contract 03PL034C) within the German ACSYS program, and by the EC Environment and Climate Research Programme (contract: ENV4-CT97-0487, Arctic Radiation and Turbulence Interaction Study).

References

Alam, A. and Curry, J. A.: 1997, 'Determination of Surface Turbulent Fluxes Over Leads in Arctic Sea Ice', *J. Geophys. Res.* **102**, 3331–3344.

Alestalo, M. and Savijärvi, H.: 1985, 'Mesoscale Circulations in a Hydrostatic Model: Coastal Convergence and Orographic Lifting', *Tellus* **37A**, 156–162.

Andreas, E. L.: 1987, 'A Theory For the Scalar Roughness and the Scalar Transfer Coefficients Over Snow and Sea Ice', *Boundary-Layer Meteorol.* **38**, 159–184.

Andreas, E. L., Paulson, C. A., Williams, R. M., Lindsay, R. W., and Businger, J. A.: 1979, 'The Turbulent Heat Flux from Arctic Leads', *Boundary-Layer Meteorol.* **17**, 57–91.

Andreas, E. L., Fairall, C. W., Guest, P. S., and Persson, P. O. G.: 1999, 'An Overview of the SHEBA Atmospheric Flux Program', in *Fifth Conference on Polar Meteorology and Oceanography*, Dallas, TX, January 10–15, 1999, American Meteorological Society, Boston, MA, pp. 550–555 (preprint).

Bennett, T. J. Jr., and Hunkins, K.: 1986, 'Atmospheric Boundary Layer Modification in the Marginal Ice Zone', *J. Geophys. Res.* **91**, 13033–13044.

Birnbaum, G. and C. Lüpkes: 2002, 'A new Parameterization of Surface Drag in the Marginal Sea Ice Zone', *Tellus* **54A**, 107–123.

Bourke, R. H. and Garrett, R. P.: 1986, 'Sea Ice Thickness Distribution in the Arctic Ocean', *Cold Reg. Sci. Techn.* **13**, 259–280.

Brümmer, B. and Thiemann, S.: 2002, 'The Atmospheric Boundary Layer in an Arctic Wintertime On-ice Air Flow', *Boundary-Layer Meteorol.* **104**, 53–72.

Brümmer, B., Busack, B., and Hoeber, H.: 1994, 'Boundary-layer Observations Over Water and Arctic Sea Ice During On-ice Air Flow', *Boundary-Layer Meteorol.* **68**, 75–108.

Cheng, B. and Vihma, T.: 2002, 'Modelling of Sea Ice Thermodynamics During Warm-air Advection', *J. Glaciol.* **48**, 425–438.

Drüe, C. and Heinemann, G.: 2001, 'Airborne Investigation of Arctic Boundary-layer Fronts over the Marginal Ice Zone of the Davis Strait', *Boundary-Layer Meteorol.* **101**, 261–292.

Fairall, C. W. and Markson, R.: 1987, 'Mesoscale Variations in Surface Stress, Heat Fluxes, and Drag Coefficient in the Marginal Ice zone during the 1983 Marginal Ice Zone Experiment', *J. Geophys. Res.* **92**, 6921–6932.

Freese, D.: 1999, 'Solar and Terrestrial Radiation Interaction between Arctic Sea Ice and Clouds' (in German), *Rep. Polar Res.* **312**, Alfred-Wegener-Institute for Polar and Marine Research, Bremerhaven, Germany, 116 pp.

Garbrecht, T., Lüpkes, C., Hartmann, J., and Wolff, M.: 2002, 'Atmospheric Drag Coefficients over Sea Ice – Validation of a Parameterization Concept', *Tellus* **54A**, 205–219.

Guest, P. S. and Davidson, K. L.: 1994, 'Factors Affecting Variations of Snow Surface Temperature and Air Temperature over Sea Ice in Winter', in O. M. Johannessen, R. Muench, and J. E. Overland (eds), *The Polar Oceans and Their Role in Shaping the Global Environment*, *Nansen Centennial Volume*, *Geophysical Monograph Series*, Vol. 85, American Geophysical Union, Washington, DC, pp. 435–442.

Guest, P. S., Glendening, J. W., and Davidson, K. L.: 1995, 'An Observational and Numerical Study of Wind Stress Variations within Marginal Ice Zones', *J. Geophys. Res.* **100**, 10887–10904.

Hartmann, J., Kottmeier, C., and Raasch, S.: 1997, 'Roll Vortices and Boundary-layer Development during a Cold Air Outbreak', *Boundary-Layer Meteorol.* **84**, 45–65.

Hartmann, J., Albers, F., Argentini, S., Bochert, A., Bonafe, U., Cohrs, W., Conidi, A., Freese, D., Georgiadis, T., Ippoliti, A., Kaleschke, L., Lüpkes, C., Maixner, U., Mastrantonio, G., Ravegnani, F., Reuter, A., Trivellone, G., and Viola, A.: 1999, 'Arctic Radiation and Turbulence Interaction Study (ARTIST)', *Rep. Polar Res.* **305**, Alfred-Wegener-Institute for Polar and Marine Research, Bremerhaven, Germany, 81 pp.

Hein, P. F. and Brown, R. A.: 1988, 'Observations of Longitudinal Roll Vortices during Arctic Cold Air Outbreaks Over Open Water', *Boundary-Layer Meteorol.* **45**, 177–199.

Intrieri, J. M., Fairall, C. W., Shupe, M. D., Persson, P. O. G., Andreas, E. L., Guest, P. S., and Moritz, R. E.: 2002, 'An Annual Cycle of Arctic Surface Cloud Forcing at SHEBA', *J. Geophys. Res.* **107**, 8039, doi: 10.1029/2000JC000439.

Jordan, R. E., Andreas, E. L., and Makshtas, A. P.: 1999, 'Heat Budget of Snow-covered Sea Ice at North Pole 4', *J. Geophys. Res.* **104**, 7785–7806.

Kottmeier, C. (ed.): 1996, *User Handbook for the Polar 2 and Polar 4 Research Aircraft*, Alfred Wegener Institute for Polar and Marine Research, Bremerhaven, Germany, 46 pp.

Lüpkes, C. and Schlünzen, K. H.: 1996, 'Modelling the Arctic Convective Boundary-Layer with Different Turbulence Parameterizations', *Boundary-Layer Meteorol.* **79**, 107–130.

Makshtas, A. P.: 1991, *The Heat Budget of Arctic Ice in the Winter*, Int. Glaciol. Soc., Cambridge, England, 77 pp.

Morcrette, J.-J.: 1991, 'Radiation and Cloud Radiative Properties in the ECMWF Forecasting System', *J. Geophys. Res.* **96**, 9121–9132.

Olsson, P. Q. and Harrington, J. Y.: 2000, 'Dynamics and Energetics of the Cloudy Boundary Layer in Simulations of off-Ice Flow in the Marginal Ice Zone', *J. Geophys. Res.* **105,** 11889–11899.

Overland, J. E. and Guest, P. S.: 1991, 'The Arctic Snow and Air Temperature Budget over Sea Ice During Winter', *J. Geophys. Res.* **96**, 4651–4662.

Overland, J. E. and Turet, P.: 1994, 'Variability of the Atmospheric Energy Flux Across 70°N Computed from the GFDL data Set', in O. M. Johannessen, R. Muench, and J. E. Overland (eds), *The Polar Oceans and Their Role in Shaping the Global Environment*, *Nansen Centennial Volume*, *Geophysical Monograph Series*, Vol. 85, American Geophysical Union, Washington, DC, pp. 313–325.

Persson, P. O. G., Fairall, C., Andreas, E. L., Guest, P. S., and Perovich, D. K.: 2002, 'Measurements Near the Atmospheric Surface Flux Group Tower at SHEBA: Near-Surface Conditions and Surface Energy Budget', *J. Geophys. Res.* **107**, 9045, doi: 10.1029/2000JC000705.

Pinto, J. O.: 1998, 'Autumnal Mixed-phase Cloudy Boundary Layers in the Arctic', *J. Atmos. Sci.* **55**, 2016–2038.

Pinto, J. O., Alam, A., Maslanik, J. A., Curry, J. A., and Stone, R. S.: 2003, 'Surface Characteristics and Atmospheric Footprint of Springtime Arctic Leads at SHEBA', *J. Geophys. Res.* **108**, 8051, doi: 10.1029/2000JC000473.

Savijärvi, H.: 1991, 'The United States Great Plains Diurnal ABL Variation and the Nocturnal Low-level Jet', *Mon. Wea. Rev.* **119**, 833–840.

Savijärvi, H.: 1997, 'Diurnal winds around Lake Tanganyika', *Quart. J. Roy. Meteorol. Soc.* **123**, 901–918.

Savijärvi, H. and Amnell, T.: 2001, 'High Resolution Flight Observations and Numerical Simulations: Horizontal Variability in the Wintertime Boreal Boundary Layer', *Theor. Appl. Climatol.* **70**, 245–252.

Savijärvi, H. and Kauhanen, J.: 2001, 'High Resolution Numerical Simulations of Temporal and Vertical Variability in the Stable Wintertime Boreal Boundary Layer: A Case Study', *Theor. Appl. Climatol.* **70**, 97–103.

Savijärvi, H., Arola, A. and Räisänen, P.: 1997, 'Shortwave Optical Properties of Precipitating Waterclouds', *Quart. J. Roy. Meteorol. Soc.* **123**, 883–899.

Savijärvi, H. and Räisänen, P.: 1998, 'Longwave Optical Properties of Water Clouds and Rain', *Tellus* **50A**, 1–11.

Schnell, R. C., Barry, R. G., Miles, M. W., Andreas, E. L., Radke, L. F., Brock, C. A., McCormick, M. P., and Moore, J. L.: 1989, 'Lidar Detection of Leads in Arctic Sea Ice', *Nature* **339**, 530–532.

Serreze, M. C., Maslanik, J. A., Rehder, M. C., Schnell, R. C., Kahl, J. D., and Andreas, E. L.: 1992, 'Theoretical Heights of Buoyant Convection Above Open Leads in the Winter Arctic Pack Ice Cover', *J. Geophys. Res.* **97**, 9411–9422.

Sturm, M., Perovich, D. K., and Holmgren, J.: 2002, 'Thermal Conductivity and Heat Transfer Through the Snow on the Ice of the Beaufort Sea', *J. Geophys. Res.* **107**, doi: 10.1029/2000JC000409.

Uttal, T., et al.: 2002, 'The Surface Heat Budget of the Arctic Ocean', *Bull. Amer. Meteorol. Soc.* **83**, 255–276.

Vihma, T.: 1995, 'Subgrid Parameterization of Surface Heat and Momentum Fluxes over Polar Oceans', *J. Geophys. Res.* **100**, 22625–22646.

Vihma, T. and Brümmer, B.: 2002, 'Observations and Modelling of On-Ice and Off-ice Air Flows over the Northern Baltic Sea', *Boundary-Layer Meteorol.* **103**, 1–27.

Vihma, T. and C. Kottmeier, C.: 2000, 'A Modelling Approach for Optimizing Flight Patterns in Airborne Meteorological Measurements', *Boundary-Layer Meteorol.* **95**, 211–230.

Vihma, T., Hartmann, J., and Lüpkes, C.: 2003, 'A Case Study of an On-ice Air Flow over the Arctic Marginal Sea Ice Zone', *Boundary-Layer Meteorol.* **107**, 189–217.

Wang, S., Wang, Q., Jordan, R. E., and Persson, P. O. G.: 2001, 'Interactions among Longwave Radiation of Clouds, Turbulence, and Snow Surface Temperature in the Arctic: a model sensitivity study', *J. Geophys. Res.* **106**, 15323–15333.